Accepted Manuscript

Impact of Geological Modeling Processes on Spatial Coalbed Methane Resources Estimation

Fengde Zhou, Guangqing Yao, Stephen Tyson

PII: S0166-5162(15)00096-8
DOI: doi: 10.1016/j.coal.2015.04.010
Reference: COGEL 2462

To appear in: *International Journal of Coal Geology*

Received date: 16 February 2015
Revised date: 23 April 2015
Accepted date: 23 April 2015

Please cite this article as: Zhou, Fengde, Yao, Guangqing, Tyson, Stephen, Impact of Geological Modeling Processes on Spatial Coalbed Methane Resources Estimation, *International Journal of Coal Geology* (2015), doi: 10.1016/j.coal.2015.04.010

Impact of Geological Modeling Processes on Spatial Coalbed Methane Resources Estimation

Fengde Zhou [a, b*], Guangqing Yao [a], Stephen Tyson [b]

[a] *Key Laboratory of Tectonics and Petroleum Resources (China University of Geosciences), Ministry of Education, Wuhan 430074, China*

[b] *School of Earth Sciences, University of Queensland, Brisbane, QLD 4072, Australia*

ABSTRACT

Spatial coalbed methane (CBM) resources estimation is based on spatial distributions of coal, coal adsorbed gas content and coal density. However, the spatial distribution of gas content can be generated via two different geological modeling processes: (1) The gas content distribution is generated by geological modeling based on the interpreted gas content at boreholes; (2) Distributions of gas content related logs or coal properties are generated firstly, then the gas content distribution is calculated based on the spatial distributions of logs or coal properties by the relationship between the gas content and logs or coal properties. This paper presents a study to compare the impact of these two processes on CBM resources estimation for coal seam No.3 (CS-3) in southeast Qinshui Basin, China. Well logs from 22 wells, laboratory data from five wells and well tops from 131 wells for CS-3 are used in log interpretation and geological modeling. The simple kriging (SK) is used to build the structural model and the coal distribution.

* Corresponding author:

Tel.: +61 7 3365 1180, fax: +61 7 3365 1277

E-mail address: f.zhou1@uq.edu.au (F. Zhou)

Weighted and unweighted omni-directional variograms for structural residual and coal thickness are calculated using an in-house program. Logs of gamma-ray (GR) and density (DEN or RHOB) are distributed in 3D by using sequential Gaussian simulation (SGS) with SK algorithm. Artificial neural network (ANN) is used to build the relationship of the measured raw gas content (RGC; gas content in raw coal basis) with the logs of GR, DEN and measured depth (MD). Then the RGC is distributed in 3D by the two geological modeling processes. CBM resources are calculated in 3D based on the cells' volume, coal density and RGC. Results show that RGC increases with increase in burial depth. Total CBM resources for the study area calculated by these two processes are similar for CS-3 but the distribution probability of high gas content is highly different which is important for locating wells.

Keywords: Coalbed methane resources; geological modeling processes; artificial neural network.

1. INTRODUCTION

In coal seams, most of CBM is adsorbed in the micro-pores of coal matrix (Gray, 1987). CBM resource is estimated as a product of coal thickness, coal density and RGC in this paper. Hence, distributions of coal, coal density and adsorbed gas content are the three basic properties for volumetric CBM resources estimation. Accurate spatial distribution estimation of CBM resource is crucial for planning and design of producing methane from coalbed. 3D geological modeling, including stratigraphic modeling, structural modeling and property modeling was used to predict the distributions of coal thickness, coal density and gas content in 3D (Zuo et al., 2009; Karacan et al., 2012;

Zhou et al., 2012; Karacan, 2013). For the gas content distribution in 3D, two processes can be used. One is that the gas content distribution is generated by geological modeling based on the interpreted gas content at boreholes; another one is that the gas content related logs or coal quality properties are distributed in 3D firstly and then the gas content is calculated or predicted in 3D by the relationship between the gas content and logs or coal quality properties.

Gas content at well boreholes is interpreted by using logs and laboratory data. However, gas content interpretation is difficult because it is impacted by lots of parameters (Faiz et al., 2007; Hemza et al., 2009), e.g. coal components (contents of ash, moisture, fixed carbon and volatile matter content), coal maceral compositions (vitrinite reflectance ratio - VRO, vitrinite, liptinite and inertinite), coal maturity, pressure and temperature, etc. In laboratory, coal adsorbed gas content, coal components, gas desorption time and coal bulk density are normally measured for each sample. Coal maceral compositions are measured in a separate experiment. Kim (1997) estimated the gas content of coals in place by integrating the pressure, temperate and the ratio of fixed carbon over volatile matter content in wt.%. Based on the desorption values for the 61 low volatile bituminous coal samples, Nolde and Spears (1998) calculated the gas content using a linear regression equation in which the depth is the only independent variable and gas content increases with increase in depth. Fu et al. (2009) estimated the gas content using multivariable regression analysis by relating burial depth, resistivity, sonic slowness and DEN with measured gas contents from 32 samples. Four of the five reported equations by Fu et al. show that the gas content increases with increase in burial depth. Karacan et al. (2012) also reported an increasing trend of gas content with increase in overburden depth and they calculated the gas content using quadratic

polynomials. Using ANN to interpret coal gas content is shortage in literature.

Geostatistical methods, which are optimal when data of the modeled parameters are stationary (mean and variance or covariance do not vary significantly in space), are normally used to generate the distributions of coal properties and coal gas content (Jakeman, 1980; Mastalerz and Kenneth, 1994; Cairncross and Cadle, 1988; Hagelskamp et al., 1988; Liu et al., 2005; Heriawan and Koike, 2008b; Beretta et al., 2010; Hindistan et al., 2010; Heriawan and Koike, 2008a; Karacan et al., 2012; Karacan et al., 2014; Karacan and Olea, 2015). SGS and ordinary kriging (OK) methods (Bohling, 2005) were used to predict the distribution of coal thickness and coal quality (Beretta et al., 2010). Geostatistical modeling also was used to analyze the uncertainty of total CBM resources (Zhou et al. 2012), gas retained amount in coal gas emission zone (Karacan et al., 2012), time-lapse gas-in-place after degasification using vertical wells (Karacan, 2013; Karacan and Olea, 2013) and effect of variogram characteristics of permeability on CBM production (Zhou et al., 2014). Combination of stochastic geological modeling and history matching was used in selecting the most probable realizations from geostatistical realizations (Karacan and Olea, 2015). Sufficient data, robust log interpretation methods and appropriate geological methods can improve the reliability of resource estimation.

In this paper, ANN is used to increase the accuracy in gas content interpretation from logs. SK is used to build the structural model and SGS is used to generate the distribution of coal logs. In practical, SGS is a spatial version of a Monte Carlo simulation procedure (Srivastava, 2013) which generates multiple equiprobable realizations for the property in question (Bohling, 2005). Because the objective of this paper is to compare the impact of modeling process on CBM resource estimation, using

SK method which is based on the known mean values of parameters is to minimize the effect of kriging method on CBM resource estimation. Gas content is distributed by the two above mentioned processes. Then CBM resources are calculated and compared. The probability distribution of high gas content away from the well location is also analyzed based on multiple realizations.

2. DATA AND METHODOLOGY

2.1 Methodology

2.2.1 Geological Modeling Processes

In order to calculate CBM resources via geological modeling, distribution of gas content has to be generated. Fig. 1 shows the two processes for generating the distribution of gas content in 3D and the calculation processes for CBM resources. In Process 1, ANN is used to generate the gas content distribution in 3D based on the distribution of DEN, GR and MD. In Process 2, the gas content at borehole is firstly estimated and then built its distribution in 3D using SGS with SK algorithm (Bohling, 2005). In both processes, the gas amount in each cell is calculated with the following equation:

$$CBMR = V_b \cdot DEN \cdot RGC \tag{1}$$

where, *CBMR* is the cells' gas amount in m^3; V_b is the cells' bulk volume in m^3; *DEN* is the cells' coal density in g/cm^3 and *RGC* is the cells' gas content in m^3/t.

2.2.2 Artificial Neural Networks

It is well established that ANN has been an effective tool in dealing with non-linear and multi-dimensional data system. Fig. 2 indicates a neural network including three

layers as input, hidden (or middle) and output. In this study, logs of GR, DEN and MD are inputs and RGC is output. Each layer is made up of a number of processing elements or neurons. The output neuron represents the reservoir properties which need to be estimated. The number of input neurons (*m*) is same as the number of input well logs to be correlated with the property. Each input neuron brings one independent variable value to the network. The neuron number (*n*) in hidden layer is determined from the trial and error. ANN algorithm could be broken down to four main steps claimed by Rojas (2005) as:

- Feed-forward computation;
- Back propagation to the output later;
- Back propagation to the hidden layer;
- Weight updates.

The algorithm is stopped when the value of the error function has become sufficiently small (Cilimkovic, 2014).

The input neurons are connected to every hidden neuron by randomly initialized weights. Then each of the output neuron receives signals from all the hidden neurons and provides a similar weighted response. A feed forward network with sigmoid hidden neurons (or activation function) and linear outputs neurons is used in fitting (Matlab, R2012b; see Fig. 2). Sigmoid activation function combines nearly linear behavior, curvilinear behavior and constant behavior which makes it used usually for hidden layer (Cilimkovic, 2014). The network is trained with Levenberg-Marquard back propagation algorithm (Matlab, R2012b; Yu and Wilamowski, 2011).

It is worth to note that avoiding overfitting or overtraining problems (Tetko et al., 1995) is important for using ANN because it leads to deterioration in predicting

properties of model and untrustworthy performance when applied to novel measurements (Piotrowski and Napiorkowski, 2013). Early stopping, noise injection, weight decay, optimized approximation algorithm have been used in literature (Piotrowski and Napiorkowski, 2013). In this study, gas content data obtained from 61 coal samples of five wells are used; method by setting a maximum iteration number of 200, nine hidden layers, 25% samples for cross validation and 10% for error limit is used to avoid overtraining or overfitting in building the ANN model.

2.2.3 Simple Kriging

Kriging is an optimal interpolation method which estimates the value for estimation point as a weighted sum of neighbouring data points (Deutsch and Journel, 1998). Weights normally decrease with increasing separation distance between the estimation point and surrounded known data points. Two methods, SK and OK are used to determine the weights (Deutsch and Journel, 1998; Bohling, 2005). For SK, the mean is known and constant. The equation is:

$$Z^*(u) = m + \sum_{\alpha=1}^{n(u)} \lambda_\alpha(u)[Z(u_\alpha) - m] \quad (2)$$

where, $Z(u_\alpha)$ are the values from neighbouring points, u_α; $Z^*(u)$ is the estimated value for estimation point u; m is the mean, which is constant over the entire domain, from all the known points; $n(u)$ is the number of neighbouring data points; $\lambda_\alpha(u)$ is the weights between neighbouring points u_α and estimation point u.

2.2.4 Sequential Gaussian Simulation

Kriging gives us an estimation of both the mean and standard deviation of the variable at each grid node (Deutsch and Journel, 1998). However, SGS first generate a "sequential" path for visiting all the unknown grid nodes by input a seed number. Uniform random probability is also generated for all unknown grids. Then SGS uses kriged mean estimate and standard deviation to build the distribution of possible values at a particular location. The simulated value for one grid is determined by the generated random probability, kriged mean and standard deviation of the variable at this grid. For example, the kriged mean and standard deviation of gas content for one grid is $10m^3/t$ and $3m^3/t$, respectively. Assuming a Gaussian distribution of gas content at this grid, the gas content distribution is shown in Fig. 3. If the generated uniform probability is 0.5, then the simulated gas content for this point is 10 m^3/t. SGS uses the simulated value as input data in kriging to estimate value for successive node according to the generated random path. Note that one random number seed generates one realization of property.

2.2 Geological Data

The study area, a producing CBM district named as South Shizhuang CBM district with an area of approximate 96 km^2, is located between the county of Qinshui and the city of Gaopin in the Shanxi Province (Fig. 4; Zhou et al., 2012; Zhou et al., 2013). The ground surface indicates a rugged-topography and a maximum 300m difference between the highest and lowest altitude. Wells were drilled firstly in those areas where are easier accessible by drilling facilities. This is the reason why most wells were drilled in three zones.

From bottom to top, the stratigraphy structure is divided into three systems

(Ordovician, Carboniferous and Permian) and five groups (Fengfeng, Benxi, Taiyuan, Shanxi and Low Shihezhi; Fig. 5). The CS-3 belongs to Shanxi group which was formed in a delta and fluvial environment. Coal was accumulated mainly in the lake plain, blocked channel and delta plain (Liang et al., 2002).

Desorption data obtained from 61 coal samples of five wells (W-1 to W4 and W-6; Fig. 4) and well logs, spontaneous potential (SP), GR, deep laterolog of resistivity (RD), shallow laterolog of resistivity (RS) and DEN from 22 wells, and correlated well-tops on CS-3 from 131 wells are used in the log interpretation and reservoir modeling. The mean RGC of the 61 samples is 9.4 cc/g with standard deviation of 3.1 cc/g. RGC was measured according to the Chinese industrial standard QB/MCQ1001-1999 and converted to the standard condition (temperature at 20°C and pressure at 1atm). Fig. 6 shows the normal quantile-quantile plot (Bancroft and Hobbs, 1986) which indicates a fairly normal distribution of RGCs from these samples.

3. RESULTS AND DISCUSSION

3.1 Structural Modeling

Measured depths on both top and bottom of CS-3 for 131 wells are correlated out and then convert to elevation by using the following equation:

$$Z_{t-cs3} = Z_{kb} - D_{t-cs3} \quad (3)$$

In this equation, $Z_{t\text{-}cs3}$ is the subsea true vertical depth (*SSTVD*) on top of CS-3, Z_{kb} is the elevation of kelly bushing, and $D_{t\text{-}cs3}$ is the true vertical depth from kelly bushing to the top of CS-3, *D* equals the measured depth (*MD*) because these are vertical wells.

The structural modeling processes are: (1) generate the horizon for top of CS-3 using kriging; (2) build the thickness distribution of CS-3 using kriging; and (3)

generate the bottom of CS-3 by combining well tops on bottom of CS-3 for the 131 wells and the thickness distribution.

In the study area, well tops of CS-3 deeps obviously from east to west. The east-west directional standardize semi-variogram (ratio of semi-variogram over variance) also continues climbing steadily beyond the global variance value which is caused by the deepening trend of well tops from east to west (Zhou et al., 2012; Bohling, 2005). In order to deal with the trend (Bohling, 2005), structural residual is used to obtain the semi-variogram. In order to obtain the structural residual, the relationship of $Z_{t\text{-}cs3}$ with well locations' coordinates is built firstly by using multivariate regression as:

$$Z_{c-t-cs3} = -739271 + 0.04 \cdot x - 0.01 \cdot y \tag{4}$$

where, $Z_{c\text{-}t\text{-}cs3}$ is the calculated structural elevation trend on top of CS-3, x and y are well locations in Universal Transverse Mercator coordinate system (UTM). Fig. 7 shows a good relationship between the measured elevation and the predicted elevation on top of CS-3. Then the structural residual is calculated as:

$$R_{t-cs3} = Z_{t-cs3} - Z_{c-t-cs3} \tag{5}$$

The structural residual ranges from -48m to 73m with average and variance of 19m and 651 m^2 respectively.

Kovitz and Christakos (2004) reported that common variogram becomes increasingly unreliable with increasing in clusteredness. Declustering weights was used to calculate the modified variogram. In study area, 97% wells were drilled in three parts (see Fig. 4). So the semi-variogram of the structural residual is calculated using two methods, weighted and unweighted. Weighted semi-variogram (de Souza and Costa, 2013) is calculated by:

$$\gamma(\mathbf{h}) = \frac{1}{2} \sum_{i=1}^{N(h)} \omega_{i(h)} \left[Z(\mathbf{x_i} + \mathbf{h}) - Z(\mathbf{x_i}) \right]^2 / \sum_{i=1}^{N(h)} \omega_{i(h)} \quad (6)$$

where, $\omega_{i(h)}$ is the occupied area of the "head" point of data point pair *i* which is used as the declustering weight.

A program is coded in Matlab™ to: (1) divide the study area into Voronoi cells for the 137 wells (Fig. 8); (2) to calculate the area of each cell; and (3) to calculate the Omni-directional semi-variograms. Fig. 9a shows the standardize semi-variogram and pair numbers. Note that six well met with karst collapse column (KCC; locations are shown in Fig. 1) are not used in calculating all semi-variograms because they were formed mainly by human activities (Wang et al., 1997). The mean and variance of the structural residual are 19m and 651m^2 respectively. Results show that the experimental semi-variograms by these two methods are similar in this case. Hence, a spherical model is used to fit the unweighted semi-variogram with sill, nugget and range of 816 m^2, 0, and 1500m, respectively (see Table 2). Based on the semi-variogram, the distribution of structural residual and variance is kriged as shown in Fig. 10. Variance which represents the uncertainty is small for the area near well locations (Fig. 10b). Note that the grid size is 50m in both x- and y-direction and no more than one well filling into one grid.

The structural elevation trend for each grid is calculated by using Eq. 4 and the x- and y-coordinate at the centre of grid. Then the finial horizon on top of CS-3 is the structural elevation trend plus kriged structural residual. Fig. 11a shows the contour map of elevation on top of CS-3. Results show that the elevation is deepening from east to west.

Thickness of CS-3 at the 131 wells ranges from 4.9m to 7.6m with mean and variance of 6.3m and 0.19m^2 respectively. Fig. 9b shows the standardize semi-

variograms and pair numbers for coal thickness of CS-3. Results show that the weighted experimental semi-variograms is fluctuant. Hence an exponential model is used to fit the unweighted semi-variogram with sill, nugget and rage of $0.20m^2$, $0.13m^2$, and 4100m respectively (see Table 2). Based on the semi-variogram, the distributions of coal thickness and variance are kriged by SK method and results are shown in Figs. 11b and 10c, respectively.

The horizon on the bottom of CS-3 is generated by combining the kriged horizon on the top of CS-3, coal thickness and well tops on the bottom of CS-3 from the 131 wells. Fig. 11c shows the final horizon on the bottom of CS-3. The zone is generated by using the horizons on both top and bottom of CS-3, and then it is sub-layered into 12 layers in vertical which leads to an average grid size 0.5m. The total number of cells is 148×240×12=426,240. Fig. 12 shows the spatial distribution of CS-3 after the structural modeling.

Based on the structural model, distribution of karst collapse column was built using the objective modeling method (Zhou et al., 2012; Petrel, 2009).

3.2 Log Interpretation on Gas Content

Table 1 lists the measured gas contents and logging values at the same depths for the 61 samples. In order to build an ANN model for gas content, the correlation coefficients between gas content and each logs are analyzed. Fig. 13 shows the relationships of gas content with logs of SP, GR, RD, RS, DEN and MD. Results show that gas content increases with increase in MD while has weak relationships with each of GR, SP, DEN, RD and RS. Considering the correlation coefficients between logs and RGC, logs of MD, DEN and GR were chosen in building the ANN model for gas

content estimation (see Fig. 2). Note that shale correction on GR and DEN logs are not considered because the gas content used in the log interpretation was measured as received basis which includes content of inorganic matter. Neuron numbers are three, nine and one for input, hidden and output layers, respectively. In training ANN, maximum number of iterations is 200 hence the algorithm will stop at this number even if an adequate result has not been reached; error limit is 10%; and 25% of input data points are used for cross validation to test the result and give the error and the remaining part is used to train the model.

Compared with the models by Zhou et al. (2012), the estimated RGCs by ANN matched better with the laboratory measured data with an incremental of 0.26 in regression coefficient from 0.42 to 0.68 (Fig. 14).

3.3 Estimation of CBM Resources

There are only 22 wells with logs of GR and DEN which are insufficient for generating good variograms. Hence, omni-directional variogram with range of 500m is used in SGS for GR and DEN based on the assumption that GR and DEN are more heterogeneity than structural residual. MD is modeled by SGS with same kriging parameters as those for the structural residual modeling. Each of GR, DEN and MD are generated by SGS with 100 realizations to analyze the uncertainty. Fig. 15 shows the histograms of MD, DEN and GR which were assumed independent variables with each other in the ANN model. Histogram for DEN has two peaks with one range from l.4g/cc to 1.6 g/cc for coal and another from 2.6g/cc to 2.8g/cc for KCC. The mean DEN is 1.7g/cc and standard deviation is 0.4g/cc (see Fig. 15a). Histogram for GR has one peak around 70API. The mean GR is 79API and standard deviation is 26API (see Fig. 15b).

Histogram for MD has two peaks with one range from 550m to 600m and another from 750m to 800m. The mean MD is 624m and standard deviation is 95m (see Fig. 15c). Fig. 15d shows the histogram of coal thickness from 137 wells. Six wells from them are drilled with KCC. The average coal thickness from the 137 wells is 6.3m with standard deviation of 0.44m. Fig. 16 shows one realization for each of DEN, GR and MD. Note that the data sets of GR, DEN, MD and RGC are assumed as stationary data in geological modeling.

Each of Process 1 and Process 2 generated 100 realizations of RGC distributions in 3D. Fig. 17 shows one realization of RGC each from Process 1 and Process 2. Results indicate that the higher values of RGC from Processes 1 are distributed mostly at the west part (Fig. 17a). This is because that west part is deeper in burial depth than east part and RGC has highest correlation coefficient with MD (see Fig. 12a). However, higher values of RGC in Fig. 17b are distributed dispersedly. The reason is because RGC distribution in Fig. 17b is built by SGS and its distribution is dominated by log interrelated RGC at well boreholes and input parameters in SGS.

Swath plot was used to display of grade distributions derived from a series of sections (Tercan et al., 2013). Each of the 100 realizations from each of the two processes is averaged in vertical. Then the 100 vertical average RGCs each of the two processes are averaged again. Fig. 18 shows the swath plots of average RGCs for six sections which locations are marked in Fig. 4a. Results show that vertical average RGCs of 100 realizations from Process 2 forms a wider belt than those from Process 1 at sections #A2, A3, B3, east parts of sections #B1 and B2. It presents a higher uncertainty for RGC by Process 2 than that from Process 1 for the area with low density boreholes and vice versa. Also it indicates that the average RGCs from the 100 realizations by

Process 1 is similar with those by Process 2 at sections #A1 through A3; while in sections #B1 through B3, RGCs from Process 1 decreases from west to east but it is quite flat for RGC from Process 2. This is because RGC is stronger related with MD, which is deeper for west part than east, in Process 1 than in Process 2.

Based on the 100 realizations of RGC, the average occurrence probabilities, with RGC greater than $8m^3/t$ for CS-3, are calculated (Fig. 19). Results indicate that most cells with occurrence probability higher than 50% are located in west part for Process 1; while for Process 2, cells with higher occurrence probability than 50% are distributed dispersedly.

Fig. 20 shows the frequency distribution of the total CBM resources from Processes 1 and 2 of 100 realizations. The average CBM resources are $6.19\times10^9m^3$ and $6.38\times10^9m^3$; standard deviations are $0.05\times10^9m^3$ and $0.06\times10^9m^3$, from Processes 1 and 2, respectively. The total CBM resources from Processes 1 and 2 are similar.

Fig. 21 shows the comparison of RGCs at borehole with depth incremental of 0.1m, (well logs), after upscaled to 0.5m in vertical and in 3D models. Results show similar RGC distributions for those two processes which is the reason caused similar total CBM resources.

4. CONCLUSIONS

In this study, 61 laboratory data from five wells, log data from 22 wells and well tops data from 131 wells are used in log interpretation, structure modeling and stochastic modeling for estimation of CBM resources. ANN model is built firstly based on measured RGC and corresponding logging values. Then, we generate RGC distributions through two processes. In Process 1, parameters of DEN, GR and MD are

simulated in 3D by using SGS firstly, and then predict the distribution of the gas content in 3D using the developed ANN model. In Process 2, we firstly estimate RGC at boreholes with the ANN model and then build the RGC distribution in 3D by SGS. Then, the predicted RGC distributions are used in CBM resources calculation. Through this study, it is concluded that the weighted and unweighted omni-directional variograms are similar for structural residual; while for coal thickness, the weighted omni-directional variogram is fluctuant while unweighted omni-directional variogram is fitted well by an exponential model. The accuracy in predicting RGC at borehole by the ANN model is higher than that by the multivariate regression method. The total CBM resource by Process 1 is similar with that by Process 2 but Process 1 predicts a higher RGC for west deeper part than east. Process 1 is better in spatial CBM resources estimation for those CBM fields where RGC is strongly related with structural depth.

Nomenclature

ANN	=	artificial neural network
CBM	=	coalbed methane
CBMR	=	coalbed methane resources
CS-3	=	coal seam No.3
GR	=	gamma-ray, API
KCC	=	karst collapse column
MD	=	measured depth, m
RD	=	deep laterolog of resistivity, Ω.m
RGC	=	raw gas content measured on as received basis, cm^3/g-coal
RHOB (DEN)	=	logging coal bulk density, g/cm^3

RS	=	shallow laterolog of resistivity, Ω.m
SGS	=	sequential Gaussian simulation
SP	=	spontaneous potential, mV
UTM	=	universal Transverse Mercator coordinate system
VRO	=	vitrinite reflectance ratio

Acknowledgement

The authors thank the China United CBM Co. for providing the data and Schlumberger for providing the license for Petrel. We also thank Dr. Karacan, Dr. Joan Esterle and two reviewers for their constructive advices and comments.

References

Bancroft, B.A., Hobbs, G.R., 1986. Distribution of Kriging error and stationarity of the variogram in a coal property. *Mathematical Geology* 18, 635-652.

Beretta, F.S., Costa, J.F., Koppe, J.C., 2010. Reducing coal quality attributes variability using properly designed blending piles helped by geostatistical simulation. *International Journal of Coal Geology* 84, 83-93.

Bohling, G., 2005. C&PE940, http://people.ku.edu/~gbohling/cpe940/. Viewed on 26th January 2015.

Cairncross, B., Cadle, A.B., 1988. Paleoenvironmental control on coal formation, distribution and quality in the Permian Vryheid formation, East Witbank Coalfield, South Africa. *International Journal of Coal Geology* 9, 343-370.

Cilimkovic, M., http://www.dataminingmasters.com/uploads/studentProjects/NeuralNetworks.pdf.

Viewed on 6th August 2014.

de Souza, L.E., Costa, J.F.C.L., 2013. Sample weighted variogram on the sequential indictor simulation of coal deposits. *International Journal of Coal Geology* 112, 154-163.

Deutsch, C.V., Journel, A.G., 1998. GSLIB Geostatistical Software Library and User's Guide, Second Edition, 1998.

Faiz, M., Saghafi, A., Sherwood, N., Wang, I., 2007. The influence of petrological properties and burial history on coal seam methane reservoir characterisation, Sydney Basin, Australia. *International Journal of Coal Geology* 70(1-3), 193-208.

Fu, X., Qin, Y., Wang, G.G.X., Rudolph, V., 2009. Evaluation of gas content of coalbed methane reservoirs with the aid of geophysical logging technology. *Fuel* 88, 2269-2277.

Gray, I., 1987. Reservoir engineering in coal seams: part 1 - the physical process of gas storage and movement in coal seams. *SPE Reservoir Engineering* 2 (1), 28–34.

Hagelskamp, H.H., Eriksson, P.G., Snyman, C.P. 1988. The effect of depositional environment on coal distribution and quality parameters in a portion of the Highveld coalfield, South Africa. *International Journal of Coal Geology* 10, 51-77.

Hemza, P., Sivek, M., Jirásek, J., 2009. Factors influencing the methane content of coal beds of the Czech part of the Upper Silesian Coal Basin, Czech Republic. *International Journal of Coal Geology* 79, 29-39.

Heriawan, M.N., Koike, K., 2008a. Identifying spatial heterogeneity of coal resource quality in identifying spatial heterogeneity of coal resource quality in a multilayer coal deposit by multivariate geostatistics. *International Journal of Coal Geology* 73, 307-330.

Heriawan, M. N., Koike, K., 2008b. Uncertainty assessment of coal tonnage by spatial modeling of SEAM distribution and coal quality. *International Journal of Coal Geology* 76, 217-226.

Hindistan, A.M., Tercan, E. A., Ünver, B., 2010. Geostatistical coal quality control in Longwall mining. *International Journal of Coal Geology* 81, 139-150.

Jakeman, L.B., 1980. The relationship between formation structure and thickness in the Permo-Triassic succession of the Southern coalfield, Sydney Basin, New South Wales, Australia. *Mathematical Geology* 12, 185-212.

Karacan, C.Ö., 2013. Integration of vertical and in-seam horizontal well production analyses with stochastic geostatistical algorithms to estimate pre-mining methane drainage efficiency from coal seams: Blue Creek seam, Alabama. *International Journal of Coal Geology* 114, 96-113.

Karacan, C.Ö., Drobniak, A., Mastalerz, M., 2014. Coal bed reservoir simulation with geostatistical property realizations for simultaneous multi-well production history matching: A case study from Illinois Basin, Indiana, USA. *International Journal of Coal Geology* 131, 71-89.

Karacan, C.Ö., Olea, R.A., Goodman, G., 2012. Geostatistical modeling of the gas emission zone and its in-place gas content for Pittsburgh-seam mines using sequential Gaussian simulation. *International Journal of Coal Geology* 90-91, 50-71.

Karacan, C.Ö, Olea, R.A., 2013. Time-lapse analysis of methane quantity in the Mary Lee Group of coal seams using filter-based multiple-point geostatistical simulation. Mathematical Geosciences 45 (6), 681-704.

Karacan, C.Ö., Olea, R.A., 2015. Stochastic reservoir simulation for the modeling of uncertainty in coal seam degasification. *Fuel* 148, 87-97.

Kim, A. G., 1977. Estimating methane content of bituminous coalbeds from adsorption data. Report No. RI 8245.

Kovitz, J.L., Christakos, G., 2004. Spatial statistics of clustered data. *Stochastic Environmental Research and Risk Assessment* 18(3), 147-166.

Liang, G., Ma, E., Zheng, L., 2002. Sedimentary environment of the coal measures strata in Jincheng Mining Area. *Journal of Jiaozuo Institute of Technology* (Natural Science) 21, 94–97 (in Chinese with English abstract).

Liu, G., Zheng, L., Gao, L., Zhang, H., Peng, Z., 2005. The characterization of coal quality from the Jining Coalfield. *Energy* 30, 1903-1914.

Mastalerz, M., Kenneth, R.W., 1994. Variations in SEAM thickness, coal type and coal quality in the Namurian succession of the intrasudetic basin (southwestern Poland). *Palaeogeography, Palaeoclimatology, Palaeoecology* 106, 157-169.

Matlab, R2012b. The MathWorks, Inc.

Nolde, J.E., Spears, D., 1998. A preliminary assessment of in place coalbed methane resources in the Virginia portion of the central Appalachian Basin. *International Journal of Coal Geology* 38, 115-136.

Petrel, 2009. Help System Information. Schlumberger Limited.

Piotrowski, A.P., Napiorkowski, J.J., 2013. A comparison of methods to avoid overfitting in neural networks training in the case of catchment runoff modelling. Journal of Hydrology 476, 97-111.

Rojas, R., 2005. Neural Networks: A Systematic Introduction. Springer, 2005.

Srivastava, R.M., 2013. Geostatistics: A toolkit for data analysis, spatial prediction and risk management in the coal industry. *International Journal of Coal Geology* 112, 2-13.

Tercan, A.E., Ünver, B., Hindistan, M.A., Ertunç, G., Atalay, F., Ünal, S., Kıllıoğlu, Y., 2013. Seam modeling and resource estimation in the coalfields of western Anatolia. International Journal of Coal Geology 112, 94-106.

Tetko, I.V., Livingstone, D.J., Luik, I., 1995. Neural network studies. 1. Comparison of overfitting and overtraining. Journal of Chemical Information and Computer Sciences 35, 826-833.

Wang, H., Li, Y., Wang, E., Zhao, Z., 1997. Strategic ground water management for the reduction of karst land collapse hazard in Tangshan. China. *Engineering Geology* 48, 135-148.

Wei, C., Qin, Y., Wang, G., Fu, X., Bo, J., Zhang, Z., 2007. Simulation study on evolution of coalbed methane reservoirs in Qinshui Basin, China. *International Journal of Coal Geology* 72, 53–69.

Yu, H., Wilamowski, B., 2011. Levenberg-Marquardt Training, Chapter 12, 1–16. Intelligent Systems, CRC Press, Boca Raton, Florida.

Zhou, F., Allison, G., Wang, J., Sun, Q., Xiong, D., Cinar, Y., 2012. Stochastic modeling of coalbed methane resources: a case Study in southeast Qinshui Basin, China. *International Journal of Coal Geology* 99, 16-26.

Zhou, F., Hou, W., Allinson, G., Wu, J., Wang, J., Cinar, Y., 2013. A feasibility study of ECBM recovery and CO_2 storage for a producing CBM field in Southeast Qinshui Basin, China. *International Journal of Greenhouse Gas Control* 19, 26-40.

Zhou, F., Yao, G., Wang, J., 2014. Effects of variogram characteristics of coal permeability on CBM production: a case study in Southeast Qinshui Basin, China. *Energy Exploration & Exploitation* 32(2), 263-279.

Zuo, J., Peng, S., Yongjun, L., Chen, Z., Xie, H., 2009. Investigation of karst collapse based on 3-D seismic technique and DDA method at Xieqiao coal mine, China. *International Journal of Coal Geology* 78, 276-287.

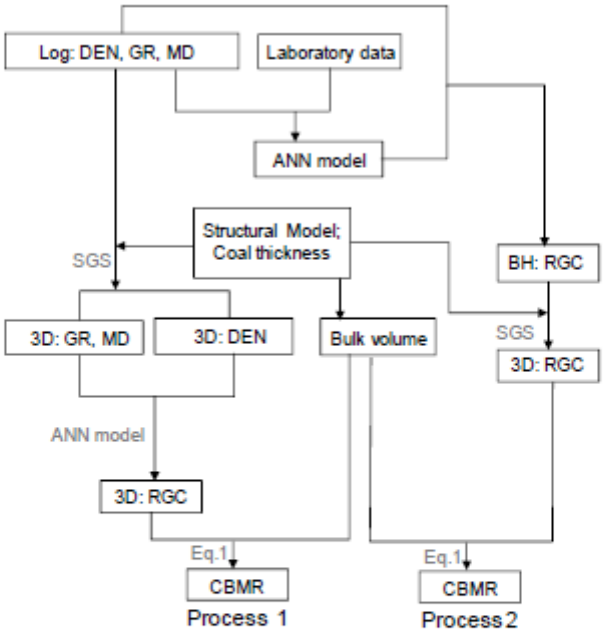

Fig. 1. Diagram showing the two different processes in CBM resources estimation (BH=borehole, 3D=three dimensions, other abbreviations are described in the text).

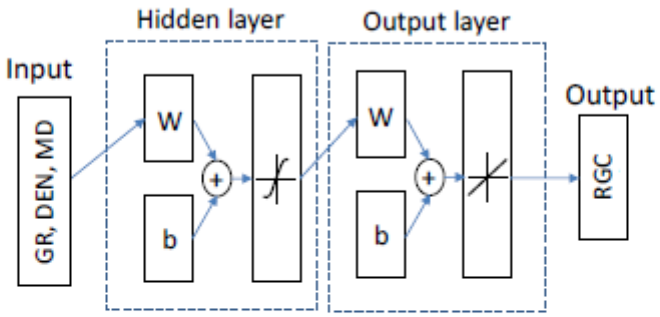

Fig. 2. A feed forward network with sigmoid hidden neurons and linear outputs neurons (after Matlab, R2012b).

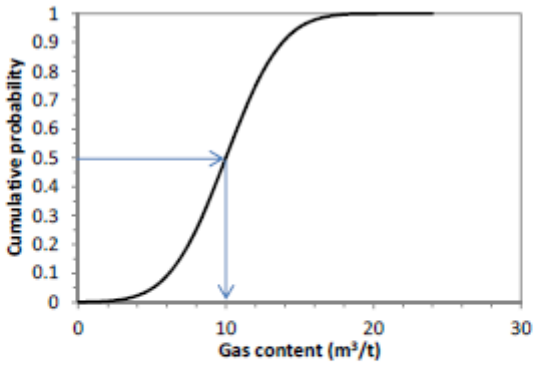

Fig. 3. Normal cumulative probability distribution of gas content with mean and standard deviation of 10 m^3/t and 3 m^3/t respectively.

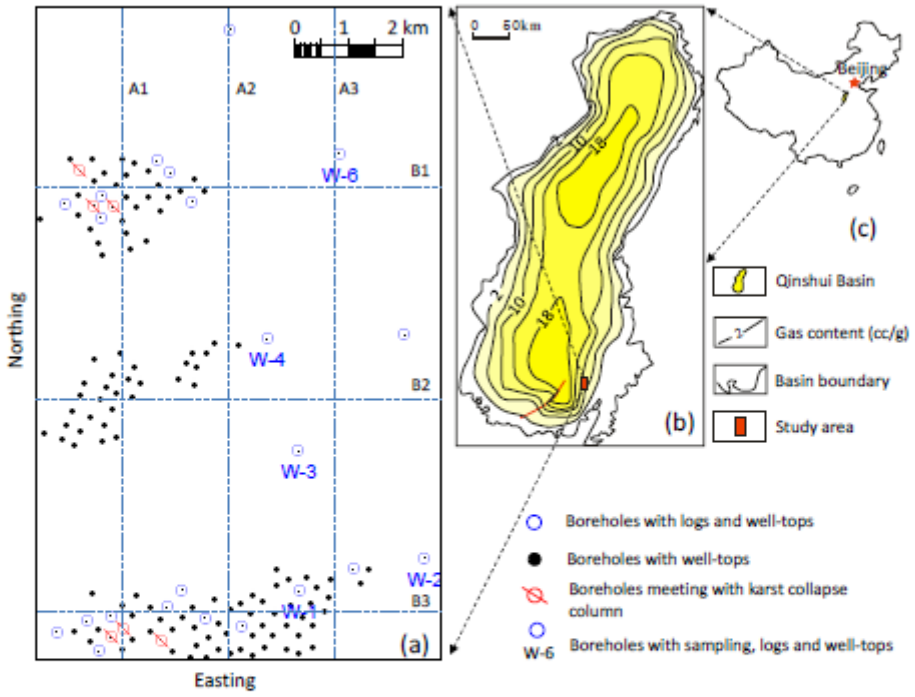

Fig. 4. Locations of (a) boreholes in (b) Qinshui basin (after Wei et al., 2007) and in (c) China. Lines A1 through A3 and B1 through B3 are sections lines for swath plots.

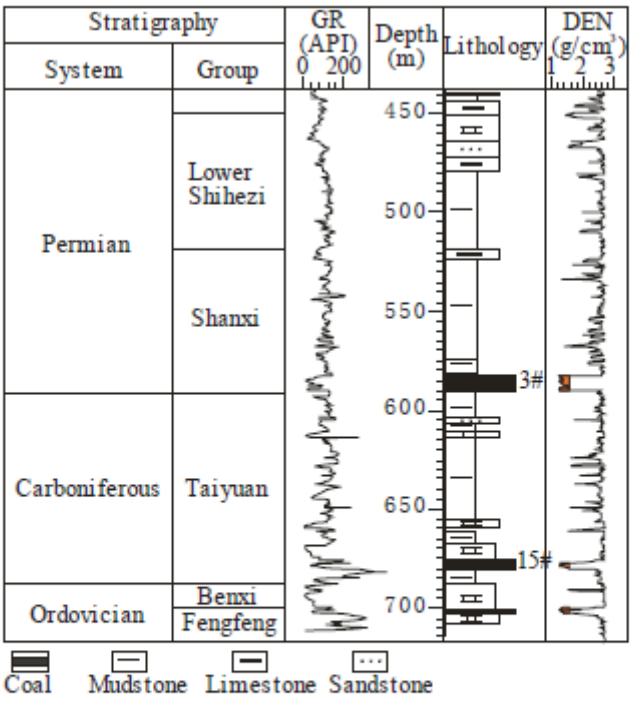

Fig. 5. Stratigraphy at well W-1 (Zhou et al., 2012).

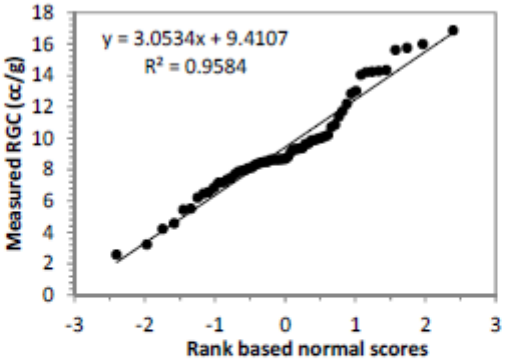

Fig. 6. Normal quantile-quantile plot of 61 points of the measured gas content.

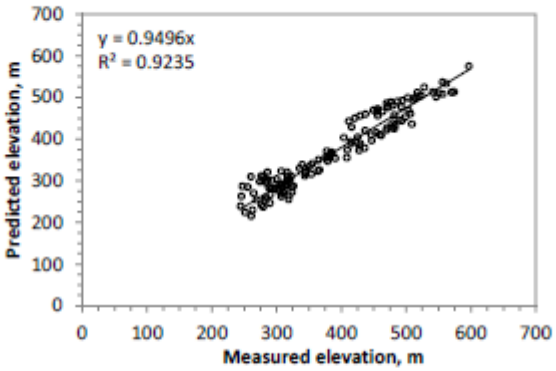

Fig. 7. Measured elevations against the predicted elevation on the top of coal seam No.3.

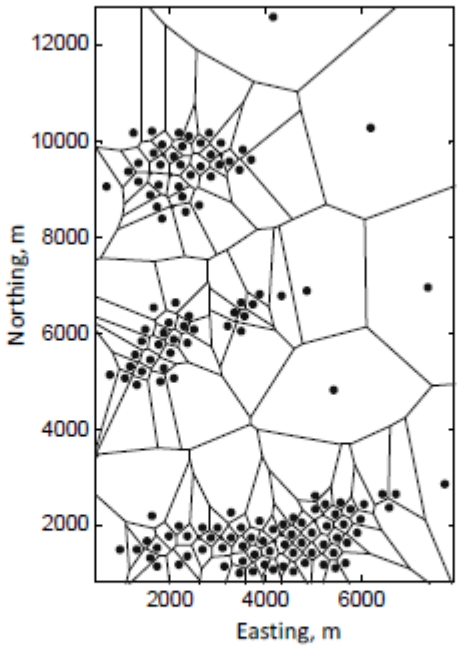

Fig. 8. Voronoi cells for the 137 boreholes used in estimation for declustering weights.

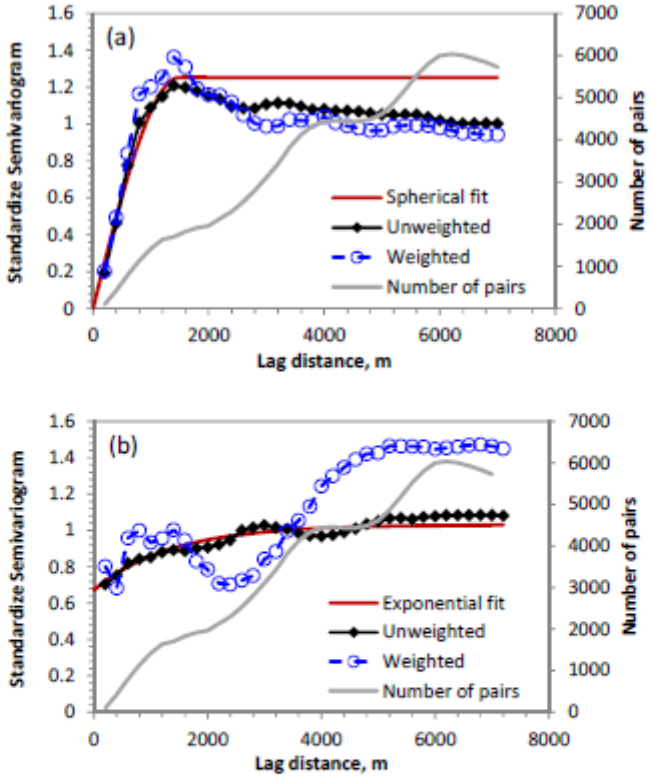

Fig. 9. Omni-directional experimental semi-variograms, variogram models and number of pair for (a) the structural residual and (b) the thickness of coal seam No.3. The experimental semi-variogram is calculated using the data of 131 wells.

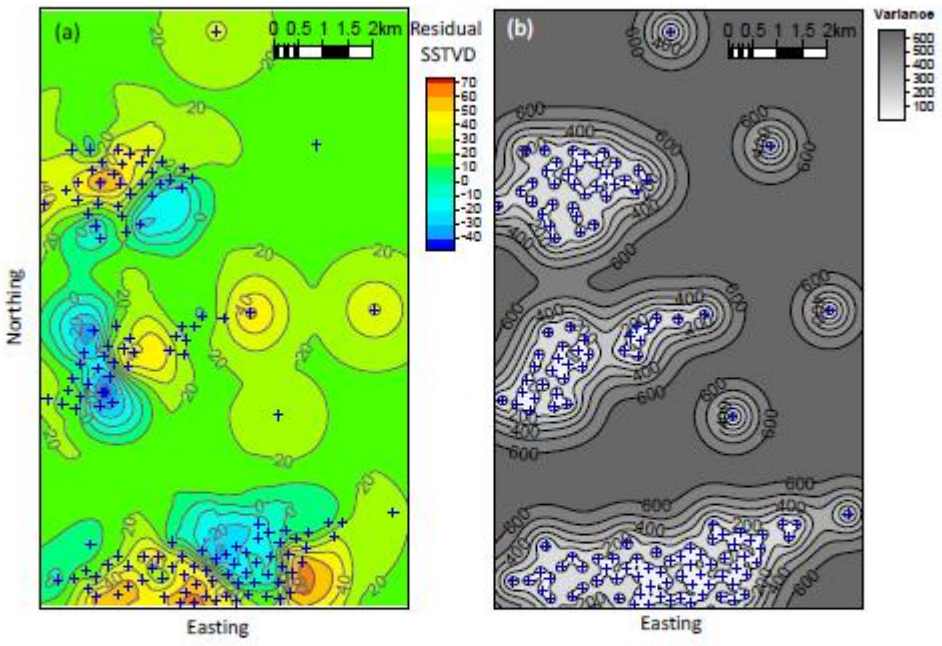

Fig. 10. Distributions of the kriged (a) structural residual and (b) variance.

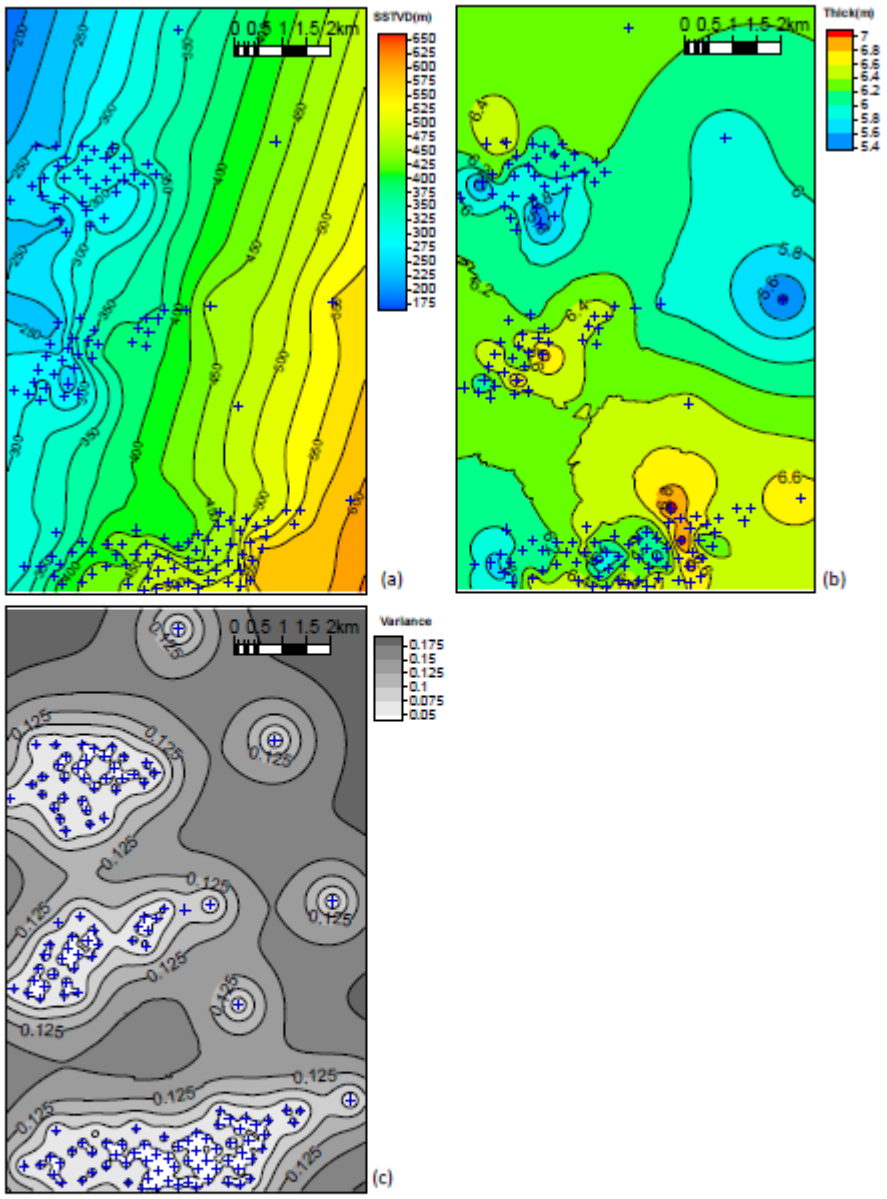

Fig. 11. (a) Contour map of elevation on top of coal seam No. 3; (b) kriged thickness of coal seam No.3 and (c) kriged variance of coal thickness. Note that positive elevation means the height above sea-level.

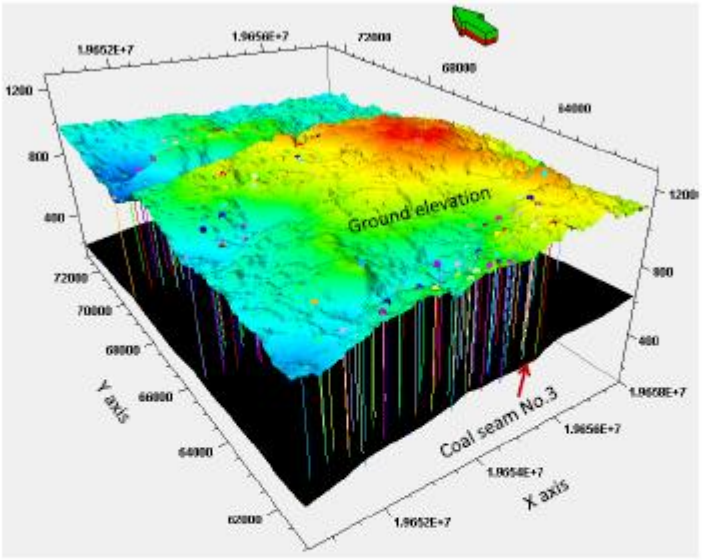

Fig. 12. Spatial distribution of coal seam No.3 after structural modeling. Ground elevation is shown as a referenced surface.

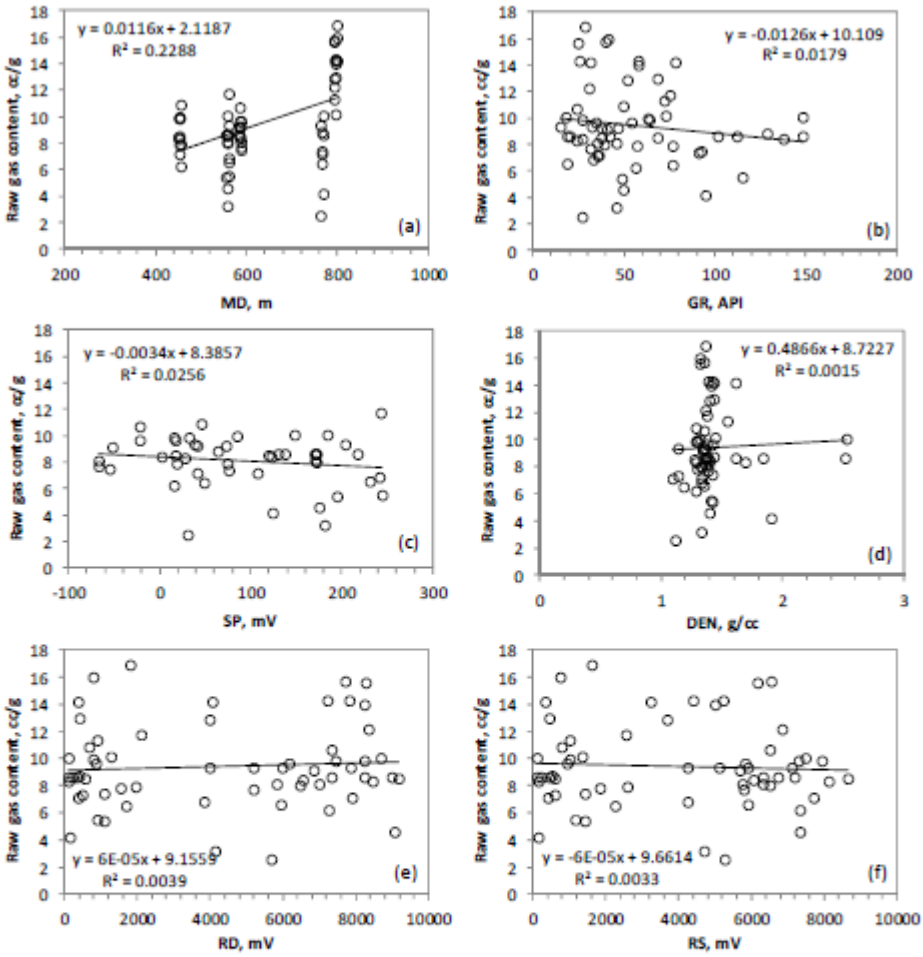

Fig. 13. Relationships of the measured gas content on received base with logs of (a) measured depth, (b) gamma ray, (c) spontaneous potential, (d) density, (e) deep laterlog resistivity and (f) shallow resistivity log.

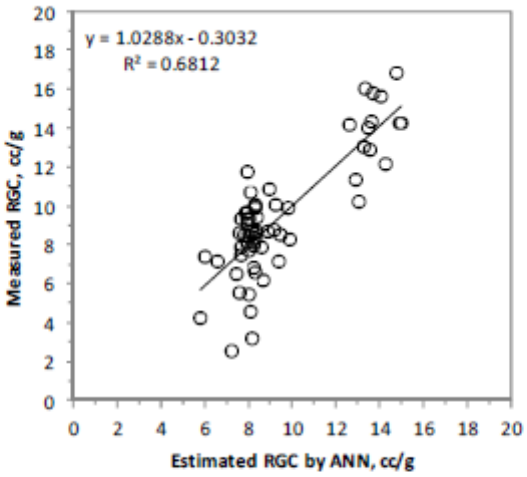

Fig. 14. Diagram shows the estimated gas content against the measured gas content on as received base.

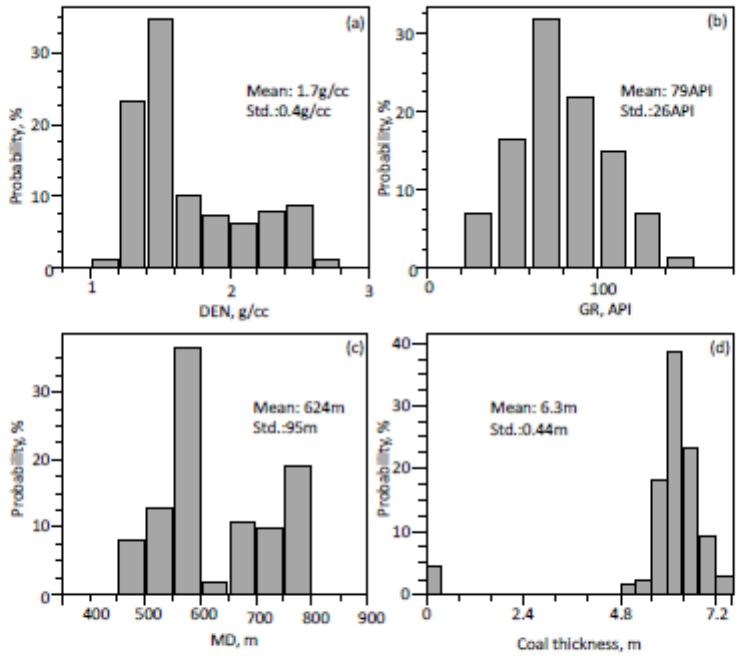

Fig. 15. Histograms for DEN (a), GR (b) and MD (c) from logs and coal thickness (d) for coal seam No. 3.

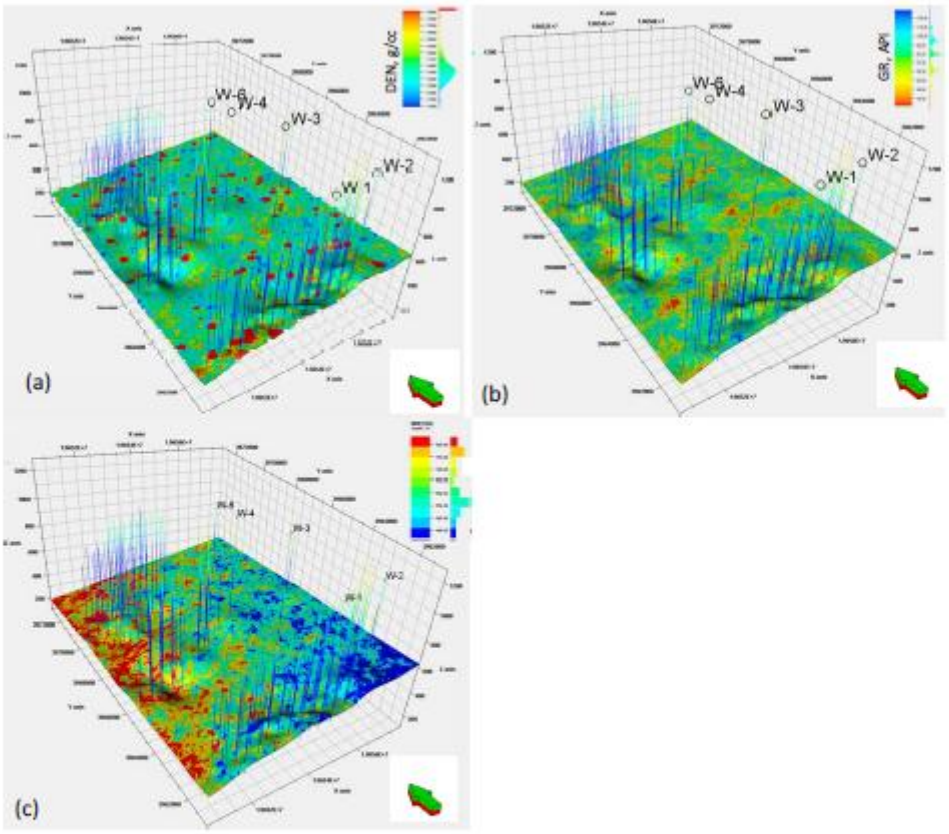

Fig. 16. One realization of (a) density and (b) gamma ray. Showing values present the values for the top grids of the 3D realization.

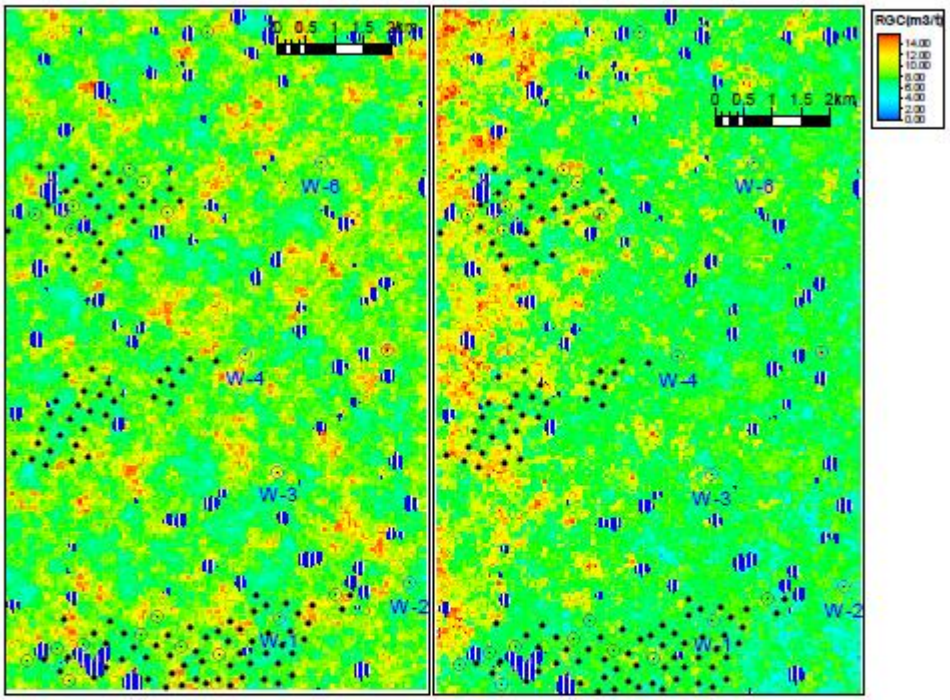

Fig. 17. Generated one realization of gas content distribution by Process 1 (a) and Process 2 (b). Showing values present the values for the top grids of the 3D realization. Near circular areas represent the predicted karst collapse column (Zhou et al., 2012).

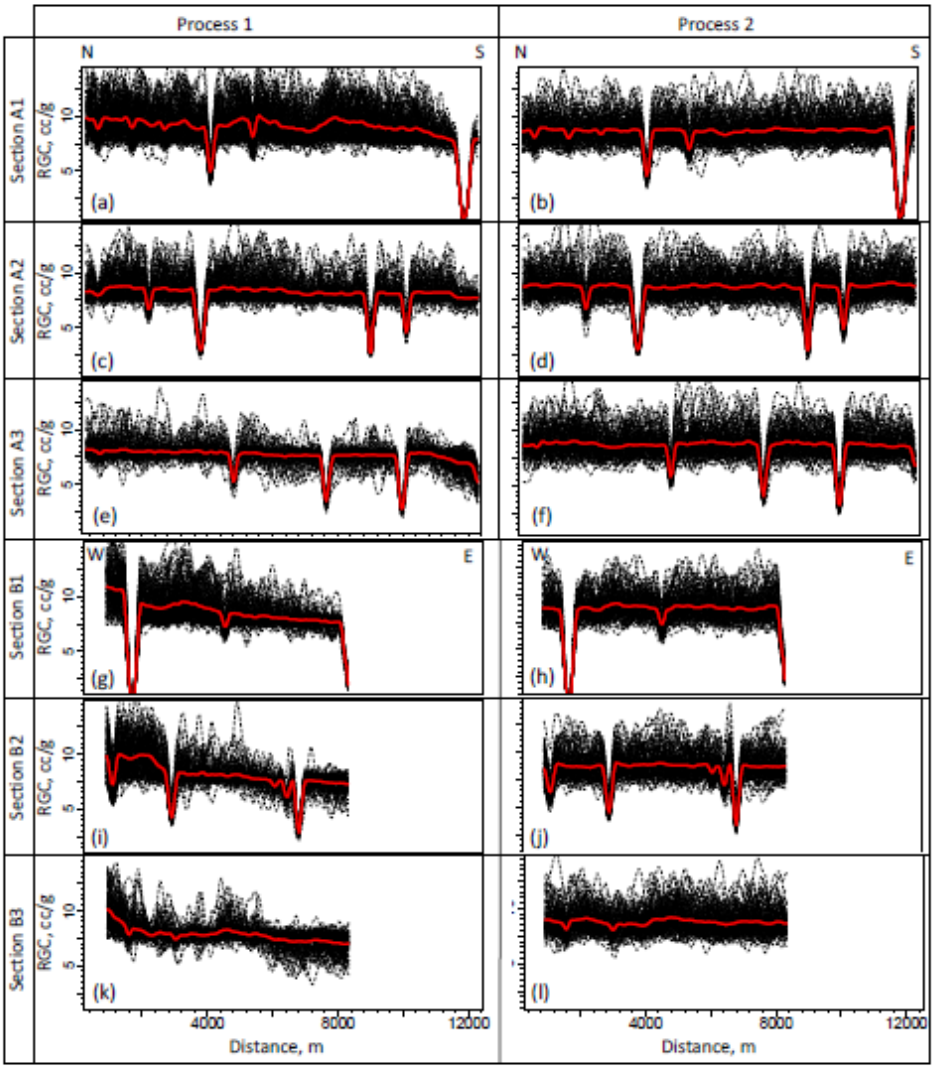

Fig. 18. Swath plots show the distribution of average RGC for coal seam No.3 along six sections (sections' locations are marked in Fig. 4). Dotted lines are vertical average RGC for 100 realizations and red thick lines are average RGC from the 100 realizations. Valley points are locations of KCC.

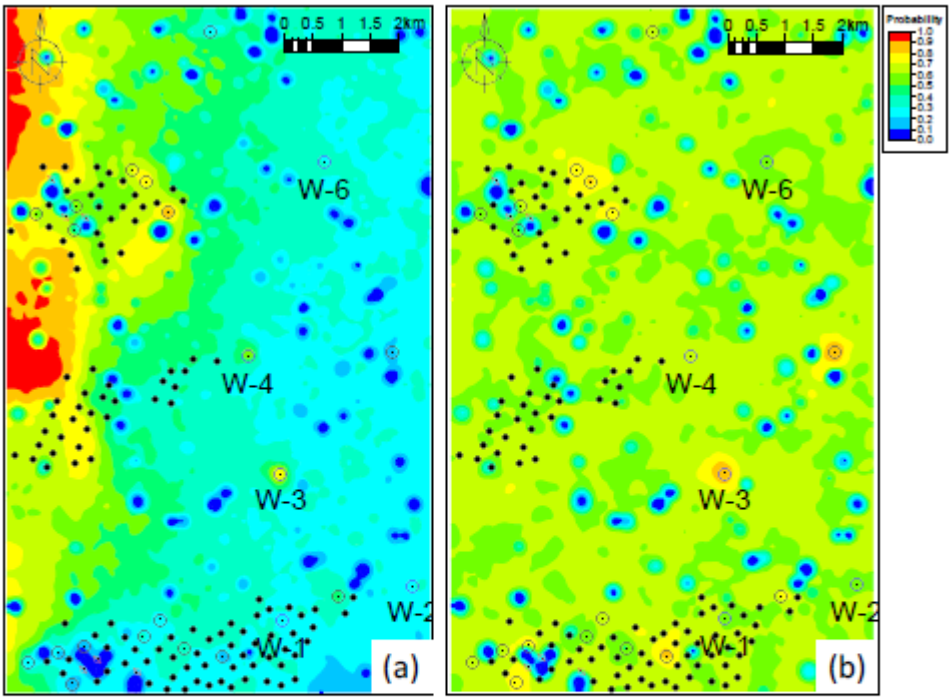

Fig. 19. Probability distribution for gas content greater than $8m^3/t$ which is calculated based on 100 realisations each from (a) Process 1 and (b) Process 2. Showing values are averages from the 12 cells in vertical.

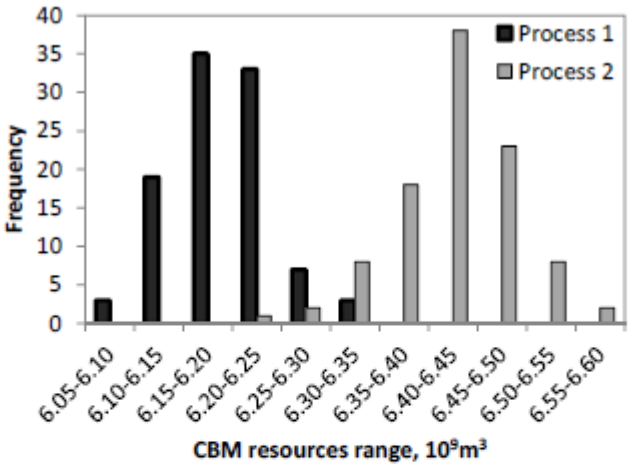

Fig. 20. Frequency distribution of CBM resources from Processes 1 and 2. The average CBM resources are $6.19\times10^{9}m^{3}$ and $6.38\times10^{9}m^{3}$; and standard deviations are $0.05\times10^{9}m^{3}$ and $0.06\times10^{9}m^{3}$, from Processes 1 and 2, respectively.

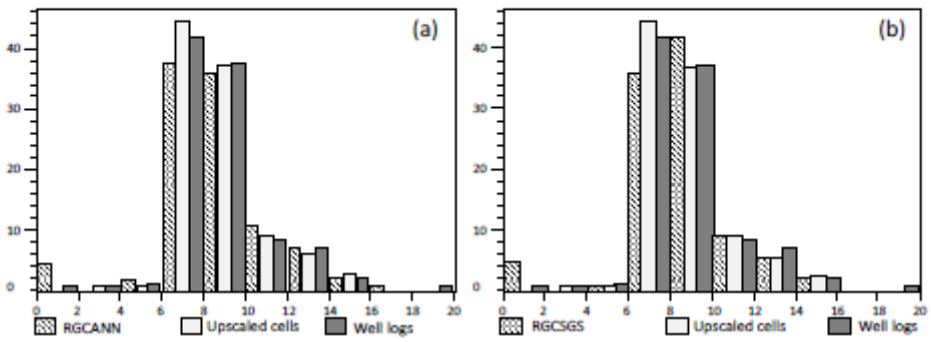

Fig. 21. Comparison of RGCs from (a) Process 1 and (b) Process 2 at wellbore with depth incremental of 0.1m (well logs), after upscaled to 0.5m (upscaled cells) in vertical and in 3D models (RGCANN or RGCSGS).

Table 1. Measured raw gas content and logging values.

SN	MD, m	GR, API	SP, mV	DEN, g/cm^3	RD, Ω.m	RS, Ω.m	RGC, cm^3/g
W1-1	583.0	112.29	129.77	1.84	223.30	236.32	8.63
W1-2	583.5	68.38	119.54	1.36	549.91	611.67	8.48
W1-3	584.3	46.95	72.72	1.36	3997.72	4233.04	9.28
W1-4	584.7	37.57	41.28	1.37	5964.68	5894.14	9.28
W1-5	585.0	34.53	17.68	1.42	6164.83	5821.74	9.64
W1-6	585.2	27.20	2.16	1.40	6526.39	6071.08	8.44
W1-7	585.5	24.29	-21.48	1.36	7324.22	6490.57	10.69
W1-8	586.0	40.47	-51.35	1.34	6846.05	5676.92	9.09
W1-9	586.7	46.20	-67.05	1.38	5828.75	5749.63	8.07
W1-10	587.0	31.61	-67.43	1.39	5184.99	5791.24	7.68
W1-11	587.6	92.38	-55.69	1.42	1090.61	1412.91	7.45
W1-12	588.4	54.49	-21.31	1.38	848.87	929.04	9.61
W2-1	450.9	137.99	121.99	1.69	115.02	131.51	8.37
W2-2	451.7	63.21	84.73	1.30	777.09	997.98	9.94
W2-3	451.9	56.94	74.44	1.30	1538.93	1859.11	7.85
W2-4	452.6	35.64	41.91	1.33	7906.55	7692.77	7.15
W2-5	452.9	27.12	32.30	1.29	8244.13	7941.87	9.85
W2-6	453.1	24.27	27.26	1.28	8459.62	8129.54	8.28
W2-7	453.8	37.71	17.22	1.27	9188.59	8633.02	8.49
W2-8	454.1	64.10	16.30	1.29	7458.65	7296.70	9.86
W2-9	454.3	56.55	16.06	1.28	7244.59	7331.59	6.2
W2-10	455.5	76.51	19.45	1.33	1940.29	2599.23	7.9
W2-11	456.4	49.47	46.15	1.29	656.93	783.83	10.84
W3-1	792.4	72.01	/	1.54	895.61	1011.74	11.35
W3-2	792.8	52.01	/	1.40	3993.74	3671.97	12.83
W3-3	793.2	39.84	/	1.36	7714.90	6526.34	15.74
W3-4	793.5	30.81	/	1.36	8342.95	6851.31	12.18
W3-5	793.9	24.80	/	1.32	8275.24	6181.81	15.6
W3-6	794.4	25.66	/	1.39	7824.58	5228.12	14.25
W3-7	794.9	57.61	/	1.41	8247.75	4990.91	14.01
W3-8	795.3	58.14	/	1.42	7208.40	4411.33	14.33
W3-9	795.8	31.78	/	1.43	4071.11	3225.64	14.22
W3-10	796.3	72.90	/	1.45	1284.36	1360.28	10.18
W3-11	796.7	68.49	/	1.44	408.06	441.50	12.99
W3-12	797.4	41.66	/	1.32	802.04	738.81	15.99
W3-13	797.8	28.68	/	1.37	1784.60	1622.37	16.86
W3-14	798.3	78.37	/	1.61	357.08	327.13	14.19
W4-1	762.8	32.44	37.99	1.13	5196.91	5119.86	9.33
W4-2	763.1	26.69	30.68	1.11	5665.98	5259.09	2.56
W4-3	765.6	76.64	48.66	1.18	1701.78	2261.43	6.46
W4-4	766.1	128.49	63.85	1.43	420.63	516.84	8.77
W4-5	766.4	90.97	76.07	1.14	485.03	610.96	7.34

W4-6	767.0	35.87	107.93	1.10	355.93	412.87	7.13
W4-7	767.3	94.83	124.05	1.91	139.48	150.53	4.2
W4-8	767.6	148.49	138.10	2.51	94.68	101.21	8.65
W4-9	768.0	148.41	147.87	2.53	99.17	107.32	10.01
W6-1	556.0	101.67	216.74	1.61	349.90	447.33	8.61
W6-2	556.4	48.84	194.34	1.42	1089.57	1436.49	5.42
W6-3	556.8	45.53	181.27	1.33	4145.76	4715.64	3.2
W6-4	557.2	39.24	172.67	1.33	6484.82	6499.76	7.97
W6-5	557.6	35.05	170.95	1.36	6978.10	6299.81	8.13
W6-6	557.9	20.17	170.14	1.38	7338.35	6303.24	8.62
W6-7	558.3	18.93	170.22	1.36	8228.93	6713.19	8.63
W6-8	558.6	42.17	171.58	1.38	8993.53	7186.33	8.65
W6-9	559.0	49.46	174.90	1.39	9067.99	7334.15	4.55
W6-10	559.4	18.30	184.03	1.32	8693.92	7493.66	10.07
W6-11	559.7	14.96	203.79	1.34	7843.14	7125.50	9.36
W6-12	560.0	18.99	231.50	1.35	5929.62	5907.65	6.56
W6-13	560.3	32.89	241.73	1.33	3829.23	4259.76	6.83
W6-14	560.6	75.40	243.48	1.38	2097.49	2552.94	11.71
W6-15	560.9	115.16	244.97	1.41	912.81	1165.31	5.5
Average	629.8	55.54	92.43	1.41	4285.80	3916.16	9.41

Table 2. Semi-variogram models and parameters for structural residual, coal thickness and logs of DEN and GR.

Properties	Semi-variogram models and parameters						
	Fitting Model	Direction	Nugget	Sill	Range	Mean	Variance
Structural residual	Spherical	Omni-direction	0	816	1500	19	651
Coal thickness	Exponential	Omni-direction	0.13	0.20	4100	6.3	0.19
DEN	Exponential	Omni-direction	0	0.16	500	1.7	0.16
GR	Exponential	Omni-direction	0	1012	500	61.7	1012
MD	Spherical	Omni-direction	0	816	1500	19	651

Note: Nugget, sill and variance are in m^2 for structural residual, MD and coal thickness; in $(g/cc)^2$ for DEN and $(API)^2$ for GR. Means are in m for structural residual, MD and coal thickness; in g/cc for DEN and API for GR. Ranges are in m.

Highlights

- Artificial neural network is used to predict gas content by logs.
- Artificial neural network is used in 3D to predict gas content distribution.
- Two geological modeling processes are used to calculate CBM resources.
- CBM resources from these two processes are compared.
- Probability distributions of high gas content from these two processes are compared.